Atomic layer deposited nanolaminates of zirconium oxide and manganese oxide from manganese(III)acetylacetonate and ozone

Atomic layer deposited nanolaminates of zirconium oxide and manganese oxide from manganese(III)acetylacetonate and ozone.

Kristjan Kalam*[1], Raul Rammula[1], Peeter Ritslaid[1], Tanel Käämbre[1], Joosep Link[2], Raivo Stern[2], Guillermo Vinuesa[3], Salvador Dueñas[3], Helena Castán[3], Aile Tamm[1], Kaupo Kukli[1].

[1]Institute of Physics, University of Tartu, W. Ostwald 1, 50411 Tartu, Estonia.

[2]National Institute of Chemical Physics and Biophysics, Akadeemia tee 23, 12618 Tallinn, Estonia.

[3]Department of Electronics, University of Valladolid, Paseo Belén 15, 47011 Valladolid, Spain.

* Corresponding author, e-mail: kristjan.kalam@ut.ee

Abstract

Atomic layer deposition method was used to grow thin films consisting of ZrO_2 and MnO_x layers. Magnetic and electric properties were studied of films deposited at 300 ºC. Some deposition characteristics of the manganese(III)acetylacetonate and ozone process were investigated, such as the dependence of growth rate on the deposition temperature and film crystallinity. All films were partly crystalline in their as-deposited state. Zirconium oxide contained cubic and tetragonal phases of ZrO_2, while the manganese oxide was shown to consist of cubic Mn_2O_3 and tetragonal Mn_3O_4 phases. All the films exhibited nonlinear saturative magnetization with hysteresis, as well as resistive switching characteristics.

Keywords: Atomic layer deposition, thin films, magnetic materials, resistive switching

Introduction

Zirconium and manganese oxide thin films have many applications, for example ZrO_2 can be used as an optical coating [1, 2], waveguide [3, 4], gas sensor [5, 6], gate dielectric in a transistor [7], functional layer of a resistive switching memory [8] and a ferroelectric memory [9, 10].

Mn-doped zirconia has also been reported to be a magnetic material [11-12]. Magnetic polarization has been achieved and studied also in Fe, Co and Ni doped zirconia [13], Ca and Mg doped [14], Ag doped [15] and even in un-doped zirconia [16-17]. MnO_2 has been used as

a catalyst [18] and an electrode [19]. MnO has been used as electrode material [20]. Mn_2O_3 has been used for water splitting devices [21].

Oxides of zirconium and magnesium have been prepared via reactive sputtering [22-23], pulsed laser deposition [1, 14, 24], electron beam evaporation [25-26], chemical vapour deposition [27-28] and spray pyrolysis [29-30].

Zirconium oxide films generally form, in atomic layer deposition (ALD) processes, possessing dioxide (ZrO_2) stoichiometry and exhibiting crystal structure characteristic of ZrO_2 polymorphs, regardless of the precursor chemistry used. For instance, ZrO_2 films have been grown by ALD using, e.g., $(CpMe)_2ZrMe_2$ or $(CpMe)_2Zr(OMe)Me$ ($Cp = C_5H_5$, $Me = CH_3$) as Zr precursors, and O_3 as the oxidant at 300 or 350 °C [31]. Growth of ZrO_2 films from $CpZr(NMe_2)_3$ and H_2O was investigated in real time at substrate temperatures ranging from 120 to 350 °C [32]. ZrO_2 growth has also been carried out using $ZrCl_4$ and H_2O as precursors [33] and a similar process has also been monitored in real time [34]. Furthermore, zirconia has been deposited from $Zr[N(C_2H_5)(CH_3)]_4$ and H_2O [9, 35].

At the same time, in the case of manganese oxide, the stoichiometry can vary, concurrently with the lattice, due to three different valences of manganese. Thus, MnO_2 has been atomic layer deposited from $Mn(thd)_3$ (thd = 2,2,6,6–tetramethyl-3,5 heptanedione) and O_3 [21, 36], MnO has also been atomic layer deposited using $Mn(EtCp)_2$, and H_2O [20], $Mn(thd)_3$ and NH_3 plasma [21], manganese(III)acetylacetonate, further denoted as $Mn(acac)_3$, and H_2O [37]. Mn_2O_3 has been obtained in the films, after annealing the as-deposited MnO_2 or MnO [21].

This study is devoted to ALD of laminated thin films consisting of ZrO_2 and manganese oxide. The purpose was to firstly investigate the process of depositing manganese oxide from ($Mn(acac)_3$) and ozone, O_3, and, thereafter, study the memory effects in nanolaminated zirconia and manganese oxide. Specifically, possible ferromagnetic, ferroelectric and resistive switching properties of such thin films were probed.

Experimental details

The films studied in this work were grown in a low-pressure flow-type ALD reactor [38]. $Mn(acac)_3$ (97%, ACROS Organics) was used as the manganese precursor and evaporated at

183 ºC. Zirconium precursor, $ZrCl_4$ (99.9 %, Aldrich), was evaporated at 157 ºC. Both metal precursors were evaporated from a glass boat inside the reactor at a pressure of 220 Pa. Nitrogen, N_2 (99.999%, Eesti AGA AS), was applied as the carrier and purging gas. Ozone was produced from O_2 (99.999%, AGA) using BMT Messtechnik 802 N generator. The ozone concentration at the reactor inlet, was 245–250 g/m^3 in the experiments. The estimated ozone flow rate from the generator was about 68 scc/m, while the carrier gas flow rate was kept at about 220 scc/m.

One ALD cycle of a binary oxide consists of four sequential pulses. For producing a layer of ZrO_2, the sequence was $ZrCl_4$ pulse – N_2 purge – O_3 pulse – N_2 purge. In the case of depositing a manganese oxide layer, the metal precursor was $Mn(acac)_3$, while purging with N_2 and oxidizing with O_3 was similar to the ZrO_2 scheme. Pulse times for depositing both metals were 5-2-2-5 s for the sequence given above. Various layered structures were deposited, for example, 100 cycles of manganese oxide followed by a 100 cycles of zirconia, more details are given in Table I.

ZrO_2-MnO_x films were grown on cleansed and etched Si(100) [39] substrate surfaces as well as on surfaces of conductive TiN layers. The TiN bottom electrode layers were pre-deposited on Si(100) wafers with a resistivity of 0.014–0.020 Ω·cm, i.e., on Si boron-doped to the concentrations up to 5×10^{18}–1×10^{19}/cm^3. TiN was grown by pulsed chemical vapour deposition using a batch $TiCl_4/NH_3$ process [40-41] at temperatures of 450–500 °C in an ASM A412 Large Batch 300 mm reactor at Fraunhofer IPMS-CNT. The films, which were deposited on TiN substrates for electrical measurements, were also supplied with Ti electrodes (area 0.204 mm^2) electron-beam evaporated on top of the films. The structure to conduct electrical measurements was, from top to bottom, Ti/ZrO_2–MnO_x/TiN/Si/Al.

Spectroscopic ellipsometer (SE), model GES5-E, was used for the measurements of the films thicknesses. Ellipsometric data was modelled in the range of 1.3-5.0 eV using the Tauc-Lorentz dispersion model. X-ray fluorescence (XRF) spectrometer Rigaku ZSX 400 and program ZSX Version 5.55 were used to measure the elemental composition of the films. Measurements were performed with a semi-quantitative (standardless analysis) program (SQX). SQX is a program to obtain concentrations of elements by theoretical calculation using the fundamental parameter (FP) method and internal sensitivity library.

The X-ray photoelectron spectra (XPS) were collected at normal emission using a Gammadata/Scienta SES100 hemispherical analyser and a Thermo VG Scientific XR3E2 non-monochromatic dual anode X-ray source (Al-K_α / Mg-K_α). The analyser energy scale

calibration was checked against the $4f_{7/2}$ line from cleaned gold foil at 84.0 eV binding energy. Relevant to estimating elemental composition from XPS survey scans, the constant (i.e., independent of photoelectron kinetic energy) analyser transmission function was checked against accessible core level lines of clean Au, Ag and Cu samples, and additionally asserted by constant magnification in spatial imaging (in the non-energy-dispersive direction) of a structured test sample through the electron optics over the entire used kinetic energy range). Spectral components were fitted, and elemental content from survey spectra was estimated using CasaXPS software [42]. XPS was exploited, in the first place, to detect the presence of carbon, complementarily to XRF, and study the differences of the carbon bonding in the films grown at two different temperatures, 250 and 300 °C, i.e. that providing the most uniform films in terms of thickness, and that probably enabling higher degree of structural ordering, respectively. No preclean or surface etching was conducted before XPS measurements, since deposition of metal electrodes was in order after the deposition of oxide films, and that could not be carried out in a continuous process without exposure to the laboratory air. Nevertheless, since the probing and analysis depth of XPS extends through topmost 4-5 nm of a film, the method allowed one to acquire data adequately, sufficient for the description of bonding between elements constituting the solid layers. Different roles for carbon impurities were expected due to the lower rate of surface exchange reactions at lower temperatures. The crystal structure was evaluated by grazing incidence X-ray diffractometry (GIXRD), using an X-ray diffractometer SmartLab Rigaku with CuKα radiation, which corresponds to an X-ray wavelength of 0.15406 nm.

Resistive switching measurements were carried out by means of a semiconductor analyzer Keithley 4200SCS, with samples put in a light-tight probe station. The DC voltage was applied to the top electrode, leaving the bottom one grounded. The current-voltage curves were measured by applying voltage sweeps while incremental voltage pulses were applied in order to obtain the memory maps seen in Fig. 12. The resistive switching measurements appropriate for recording common current-voltage hystereses as well as those enabling admittance memory mapping have been described in a number of earlier studies, e.g., those devoted to HfO_2 [43] and ZrO_2-Al_2O_3 [44] based media. The aforementioned semiconductor analyzer can also be used to perform the Double Swing Quiescent Current (DSQC) technique [45], a novel method which would allow one to detect the polarization curves of thin film samples implying ferroelectric behaviour.

Magnetic measurements were performed using Vibrating Sample Magnetometer (VSM) option of the Physical Property Measurement System 14T Quantum Design by scanning the magnetic field from -0.5 to 0.5 T parallel to the film surface at 300 K and -3.5 to 3.5 T at 5 K.

Results and discussion

Film growth and composition

Data regarding the composition of films is given in Table I. Since the zirconium precursor contains chloride and the manganese precursor contains carbon, amounts of these elements were measured as well.

Table I. Thicknesses and manganese contents for studied samples with given process descriptions. Deposition temperature was 300 °C.

Process description	Thickness, nm	Mn/(Mn+Zr)	Cl, at. %	C, at. %
200 x ($ZrCl_4$+O_3)	26	0	0.7	-
200 x ($Mn(acac)_3$+O_3)	50	1	-	33
100 x ($Mn(acac)_3$+O_3) + 100 x ($ZrCl_4$+O_3)	20+16 (MnO_x + ZrO_2)	0.6	0.6	11
50 x ($Mn(acac)_3$+O_3) + 50 x ($ZrCl_4$+O3)	7+7 (MnO_x + ZrO_2)	0.6	0.4	28
50 x ($Mn(acac)_3$+O_3) + 50 x ($ZrCl_4$+O_3) + 50 x ($Mn(acac)_3$+O_3) + 50 x ($ZrCl_4$+O_3) + 50 x ($Mn(acac)_3$+O_3)	7+7+7+7+7 (MnO_x + ZrO_2 + MnO_x + ZrO_2 + MnO_x)	0.7	1.3	11

Certain issues became related to the uniformity of the film thickness along the gas flow direction in the flow-type reactor used in the experiments. For $ZrCl_4$ as the Zr precursor in ALD, it is known, that this particular precursor does not decompose thermally even at elevated temperatures. Even at the substrate temperature of 500 °C, the thickness of ZrO_2 films grown from $ZrCl_4$ and H_2O may not deviate more than 12-15 %, measured along the substrate length [46]. Formation of certain thickness profile in chloride based ALD processes is probably inevitable in such flow-type reactors, possibly caused by the effect of secondary surface reactions, i.e., „poisoning“ of the surface by reaction products, that is HCl [47]. However, in the case of organic and oxygen-containing ligands to metals in the precursors

like acetylacetonates, the thermal decomposition of the precursor can start in the gas phase during its transport in the reactor towards substrates, and, in this case at already slightly above 300 °C, the oxide layer may, thus, deposit with higher rate, and preferentially, to the regions closer to the leading edge of the substrate. This has, evidently, became a considerable issue in the case of the manganese oxide process, as can be seen in the Figure 1.

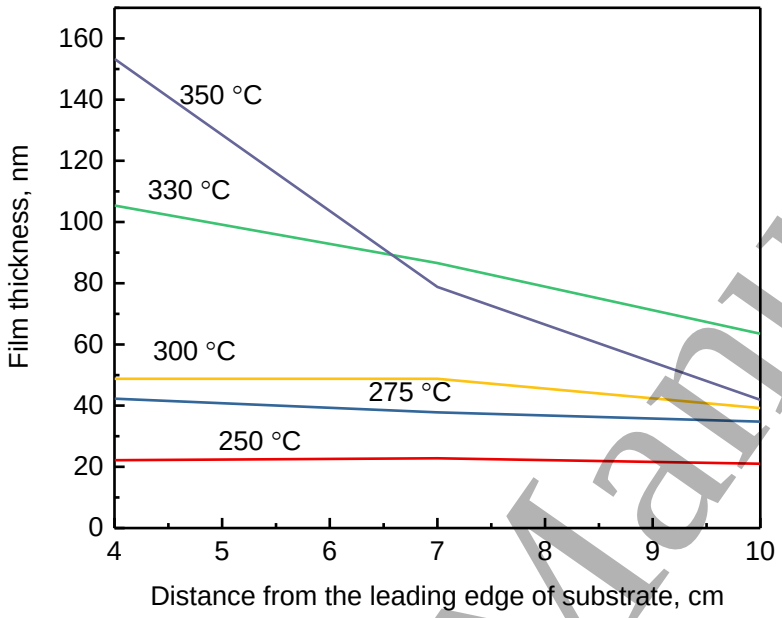

Figure 1. Manganese oxide film thicknesses using 200 ALD cycles at various deposition temperatures.

The XPS studies on elemental composition of the surface region of the films deposited at two different deposition temperatures 300 and 250 °C from XPS survey spectra revealed O:Mn content ratio approximately 1.4 for the film grown at 300 °C, similarly to the value obtained by XRF. For the film grown at 250 °C, this content ratio increased up to 2.5 and, considering the probability of formation of surface carbonate instead of oxide, increasing with decreasing substrate temperature due to incomplete reactions, the results obtained from the film grown at 250 °C could be interpreted via 3-4 nm thick surface layers dominantly consisting of $MnCO_3$ (Fig. 2).

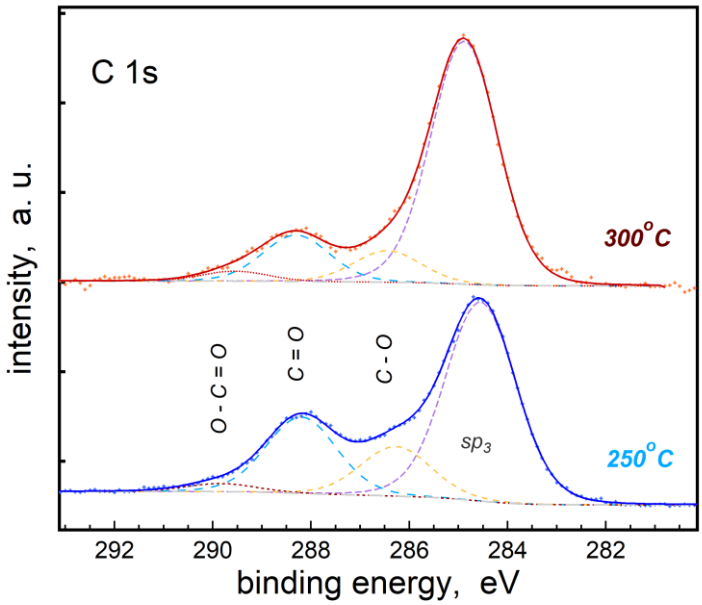

Figure 2. XPS results indicating the difference in contributions of residual carbon to the composition of manganese oxide films deposited at 250 and 300 °C.

The Mn 2p spectrum (Fig. 3), although at least partially demonstrating formation of solid manganese oxide in the present study, is generally not convenient to use for the identification of the Mn charge state due to the underlying ($2p^1$-3d final state) multiplet and nontrivial spectral structure, but the main peak maxima positions suggest 2^+ and/or 3^+ Mn charge states, and the satellite peak (Fig. 3) at binding energies ~5 eV higher than the main lines (in the 250 °C deposited sample spectrum) can be regarded as that typical of Mn^{2+} [48]. The films grown at 250 °C remained highly disordered. Multiphase structure started to form and become detected by X-ray diffraction studies or films deposited at 300 °C. The main diffraction maxima were attributed to tetragonal Mn_3O_4, while Mn_2O_3 was identified as an additional phase (Fig. 6), as will be described below. Both GIXRD and Mn 2p XPS implied that the phase composition of the MnOx films grown in the present study, especially at lowered temperatures, are complicated to define unambiguously (some further insight is provided from Mn 3s XPS, below). Besides, although manganese can take on all charge states from +7 to -3, the most abundant (and stable) oxides have charge states +2, +3 and +4, and the formula Mn_3O_4 can sometimes be written as $MnO{\cdot}Mn_2O_3$, although such physical mixture picture would imply exchange interactions such that the magnetic properties would be that of an antiferromagnet (even at low temperatures), different from what we observe (below).

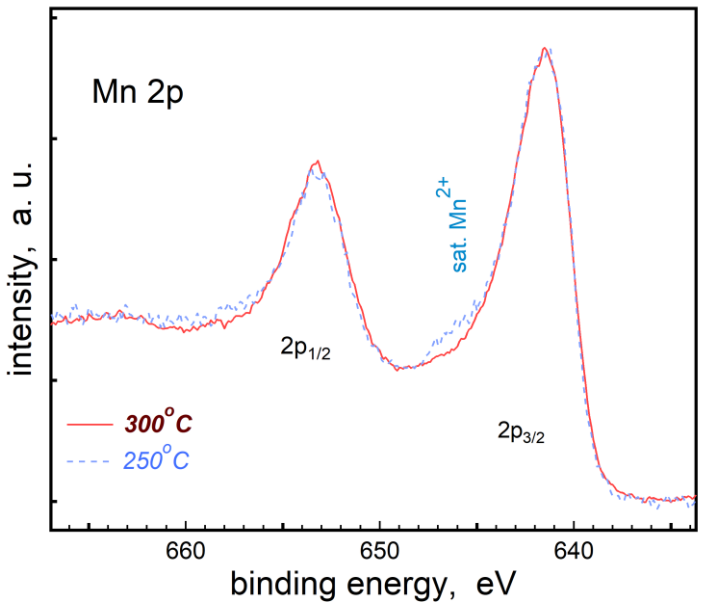

Figure 3. XPS results decribing the bonding of manganese cations in manganese oxide films deposited at 250 and 300 °C.

Figure 4 depicts oxygen 1s spectra obtained from the same reference films grown at temperatures of 250 and 300 °C. The XPS spectrum for O 1s acquired from the film grown at 300 °C demonstrated a dominant sharp peak at 529.9 eV, which is a value typical of bulk manganese oxides [49-51]. In addition, a shoulder structure was resolved and centred around 531.5 eV, which has been related to the presence of (surface) hydroxyl groups [52], accompanied by a smaller amount of C-O bonded impurity with the component peak above 532 eV and a trace peak above 533 eV. The latter could be associated to physisorbed water vapour. However, the signals detected in the spectral region in the range of 531-534 eV would also accommodate and reveal double-bonded carbon of carbonates [53-54] and/or ketonate ligands [55], likely arising from the residues of the metal precursor also exploited in the present study, amply present in the film grown at 250 °C.

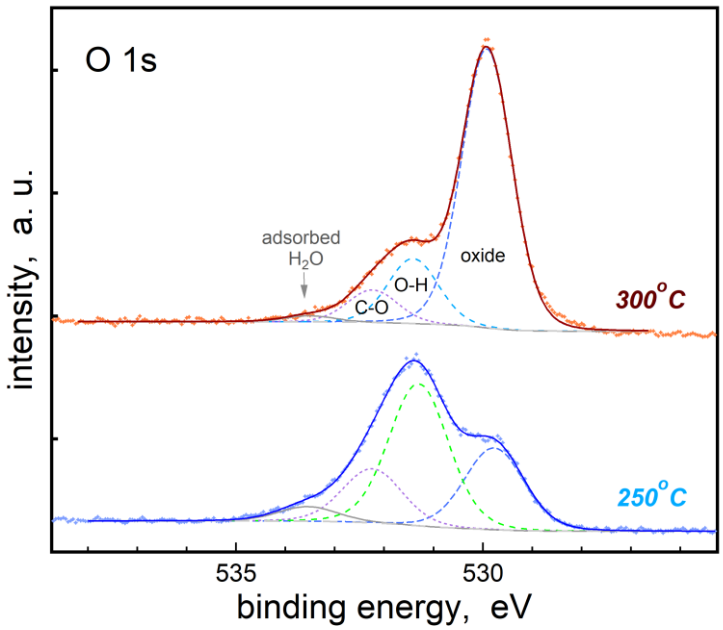

Figure 4. XPS spectra from manganese oxide films deposited at 250 and 300 °C.

The multiplet (exchange) splitting in the Mn 3s [56] due to the remaining single 3s electron in the final state having spin either parallel or antiparallel to the aligned spins of the 3d valence electrons has allowed to distinguish less ambiguously between the different Mn charge states. The size of this splitting depends also on the type of bonding (hybridisation) and typically stays at less than half of the theoretically estimated value of ~13 eV [57]. It is experimentally observed to range from 4.3 eV for Mn^{4+} to ~6 eV for Mn^{2+} [50, 58]. The Mn 3s splitting measured in the present study (Fig. 5) exhibited a peak separation of 5.9 eV for the film deposited at 300 °C. The spectral shape occurred virtually identical to that of bulk Mn_3O_4 measured earlier [58]. In the present study, the observation is also supported by the GIXRD results, allowing one to consider the Mn_3O_4 as dominant crystalline phase in such films. One can note that separation of the peaks in the measured photoelectron spectrum appears to differ significantly from those in the dominantly Mn^{3+} containing model compounds [58-59]. At the same time, the spectrum measured from the film grown at 250 °C possessed quite a similar shape (Fig. 5), but the peak separation is perceptibly, even if by as little as 0.1 eV, larger, and the lower binding energy component at 83 eV narrower, which is consistent with the features characteristic of a material containing significant amounts of $MnCO_3$, as deduced from estimates from C 1s and O 1s XPS above.

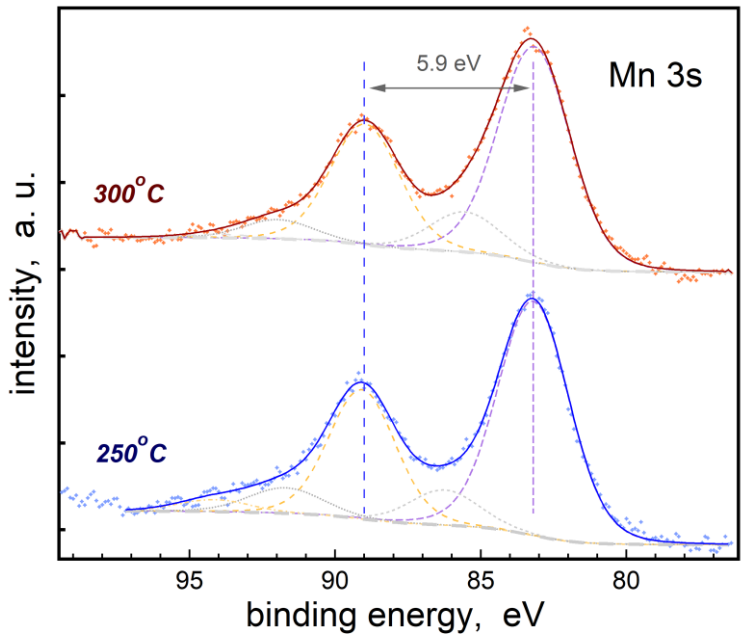

Figure 5. X-ray photoelectron spectra for Mn 3s lines measured from manganese oxide films grown at 250 and 300 °C.

In further experiments aiming at tailoring oxides of manganese and zirconium, the MnOx growth process was carried out at 300 °C, providing films with acceptable thickness uniformity and with much less carbon residues. In reference growth experiments, 200, 100, and 50 ALD cycles of manganese oxide at 300 °C resulted in films thicknesses of 50, 20, and 7 nm, respectively. This implies that the growth of the film was not linear against the amount of the deposition cycles, but increased from 0.14 to 0.25 nm/cycle. Most likely this is caused by the inhibited nucleation in the early stage of the film growth, whilst after certain film thickness e.g. number of cycles, the linear growth begins. The initial nucleation determines the structure formation and hence the film properties, which in turn is dependent on the type of substrate and its surface functionalization, precursor chemistry and deposition temperature used in ALD process. The composition measurements allowed one to state that the value of x for MnO_x was around 1.4, irrespectively of the thickness.

Film structure

As mentioned above, in MnO_x films x=1.4, measured by XRF, implying the formation of a mixture of crystalline compounds with different stoichiometry. The GIXRD studies of films deposited at 300 °C revealed, that both the cubic phase of Mn_2O_3 (PDF Card 01-078-0390) and tetragonal phase of Mn_3O_4 (PDF Card 00-018-0803) were present in the manganese oxide films not combined with ZrO_2 (Fig. 6). Moreover, one diffraction maximum attributable to

tetragonal MnO_2 (PDF Card 01-072-1982) could be recognized, although the appearance of a solitary reflection is not enough to confidently claim the corresponding phase actually formed in the films. ZrO_2 was found to be formed as a mixture of cubic (PDF Card 01-077-3168) and tetragonal (PDF Card 01-075-9649) phases. These phases can be difficult to distinguish, since several diffraction maxima tend to overlap. However, the 211 reflection of the tetragonal ZrO_2 polymorph was unambiguously recognized (Fig. 6), neighbouring the closely located 311 reflection of the cubic ZrO_2. The intensities of diffraction maxima are somewhat correlated to the thickness of films, whereby multi-layered structures demonstrating less intense maxima than those observed in non-laminated reference films, since their thicknesses are lower as well.

For a comparison with literature data, Mattelaer et al. [21] have demonstrated the possibility to control phase composition of ALD-grown manganese oxides by applying either $Mn(thd)_3$ and O_3, or $Mn(thd)_3$ and NH_3 plasma as precursors, followed by annealing the as-deposited MnO or MnO_2 films either in reducing or oxidative ambient in the temperature range of 450-900 °C. Nilsen et al. [36] have grown MnO_2 films by ALD also from $Mn(thd)_3$ and O_3 at 186 °C in a flow type ALD reactor. In the latter study, additional test experiments revealed that Mn_3O_4 could be grown at 200 °C using O_3 under atmospheric pressure, otherwise the Mn_3O_4 was achieved after increasing the substrate temperature above 230 °C. In addition, Ghods et al. [37] have obtained MnO thin films by ALD at substrate temperature of 200 °C using $Mn(acac)_3$ and H_2O as precursors. In the latter study, the stoichiometry of MnO was determined by X-ray photoelectron spectroscopy.

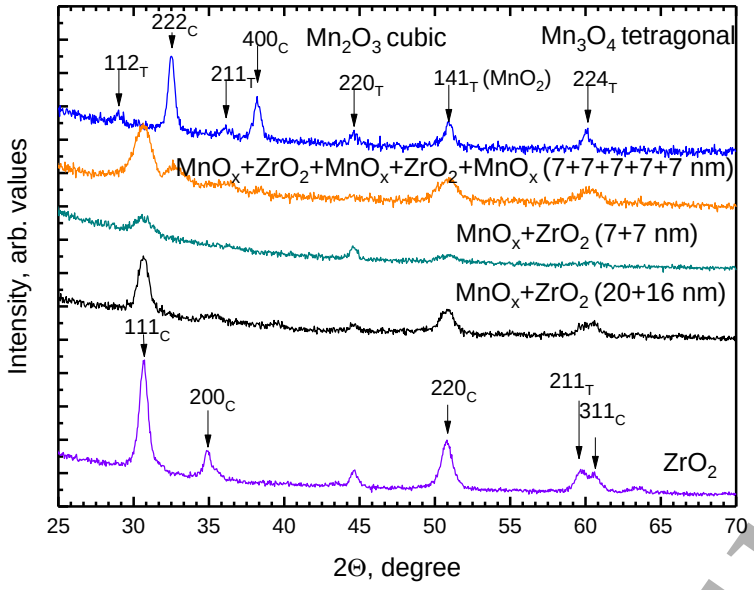

Figure 6. GIXRD diffractograms of selected multi-layered structures as well as reference zirconia and manganese oxide films, denoted by the labels. Miller indices of diffraction maxima are given for all distinct maxima, whereby T and C denote the tetragonal and cubic phase, respectively. Thicknesses of ZrO_2 and manganese oxide reference films were 26 and 50 nm, respectively

Electrical and magnetic properties

The films demonstrated nonlinear saturative magnetization with hystereses and moderate but measurable coercive fields similar to those common for ferromagnetic materials. Notably, Figure 7 shows room temperature ferromagnetic-like behaviour, most markedly apparent in the thinnest nanolaminate, with a saturation value of $1.5 \cdot 10^{-6}$ emu. Similar magnetic moment values in ZrO_2 films and its laminated structures with other metal oxides have been obtained by various authors [39, 60-61].

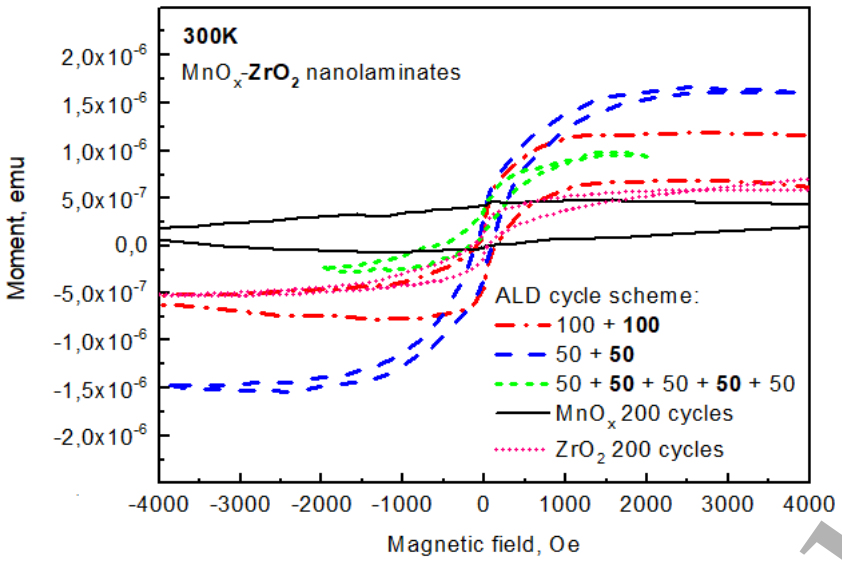

Figure 7. Magnetic moment versus external magnetic field graphs of the samples at 300 K. The amounts of ZrO_2 deposition cycles are given in bold.

There are several manganese oxides known to have magnetic ordering at lower temperatures. Worth mentioning are antiferromagnetic Mn_2O_3, Mn_5O_8 and MnO with Neel ordering temperatures of 75 K, 131 K and 115 K respectively, and ferrimagnetic Mn_3O_4 with Curie point around 46 K [62-64].

The most prominent feature from our temperature dependent zero field cooled (ZFC) and field cooled (FC) magnetization measurements is the bifurcation (irreversibility) of ZFC-FC loops and a large increase in magnetization below 46 K (Fig. 10), which coincides with the Curie temperature of Mn_3O_4 and clearly indicates the presence of the ferrimagnetic oxide in all four of the samples. No cusp or maxima in ZFC-FC curves indicating any of the antiferromagnetic (AFM) transitions could be detected. If the AFM phases exist in the samples, then their magnetic moment is below the sensitivity level of the PPMS VSM used in the measurements. Temperature dependent susceptibility of the pure ZrO_2 was flat and featureless, appropriate for a diamagnetic material.

Low temperature magnetic isotherm or hysteresis loops measured at 5 K only confirmed the existence of Mn_3O_4 in all of the samples. The coercive field (H_c) measured was 10.1 kOe for the non-laminated MnO_x film as well as for most laminates (Fig. 8 and 9). It was slightly higher for the 50+50+50+50+50 film at about 11.5 kOe (Fig. 9). Such high values of H_c have previously been reported for Mn_3O_4 nanoparticles with small crystallite sizes. [65] Figure 9 is

the same as Figure 8, but with the manganese oxide film excluded, since the saturation magnetization value for manganese oxide is so high that other samples are barely distinguishable on the graph in Figure 8.

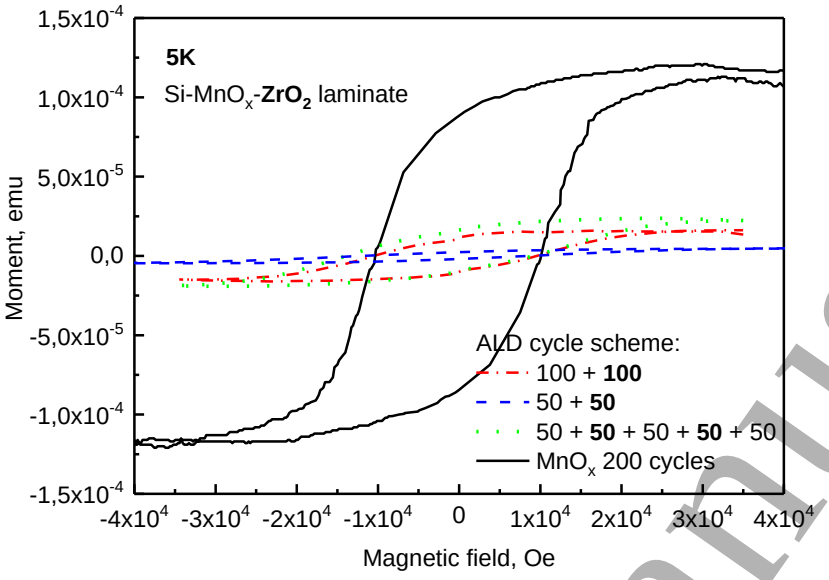

Figure 8. Magnetic moment against external magnetic field curves of all the MnO_x and ZrO_2-MnO_x films measured at 5 K.

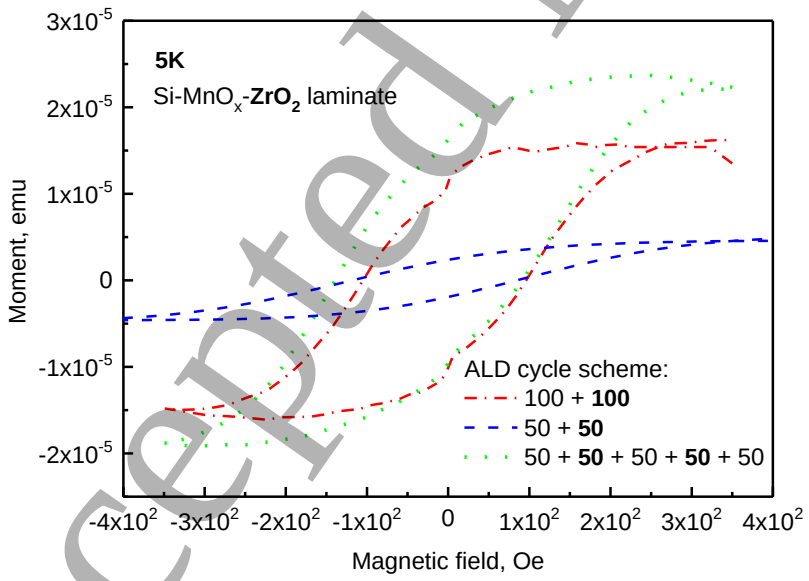

Figure 9. Magnetic moment against external magnetic field curves of the ZrO_2-MnO_x samples at 5 K. Manganese oxide film has been excluded from this image.

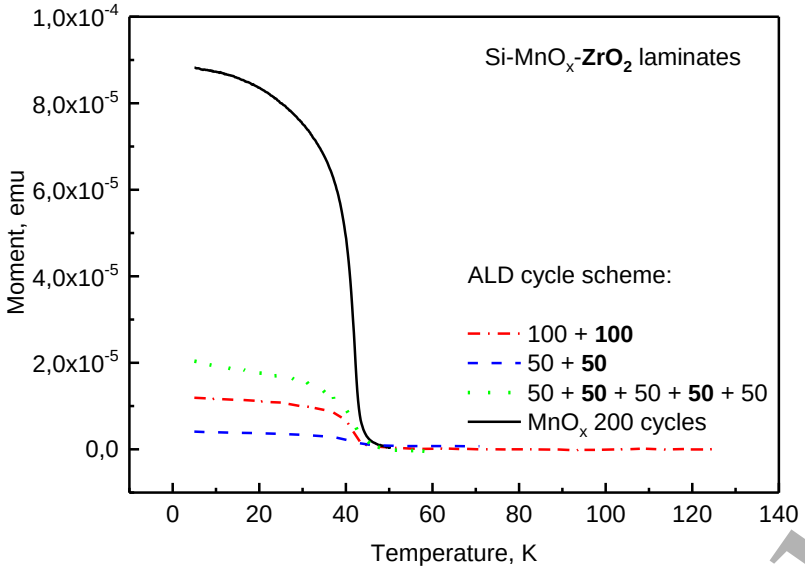

Figure 10. Magnetic moment - temperature dependence for MnO_x-ZrO_2 and MnO_x films.

All films exhibited resistive switching (RS) characteristics (Fig. 11). This means that, under electrical stimulus, these samples change their resistance state and retain its value even when the power is turned off (non-volatile effect). It has earlier been established that the physics associated with RS involves the movement of both ions and electrons [66]. Furthermore, these devices require an electroforming step [67], an initial electrical stress necessary to activate the switching property. After this process, the characteristic RS current-voltage (I-V) curves can be obtained. Bivalued curves which present two distinctive conduction states referred to as the high-resistance (HRS) and the low-resistance (LRS).

The pure (non-laminated) MnO_x and ZrO_2 samples presented the widest functional windows (Fig. 11-a and 11-b), along with the 50 x MnO_x + 50 x ZrO_2 (50+50 sample/film), which was the thinnest film as grown. The window narrowed as the number of cycles increased, as we can see when comparing the 50+50 and the 100 x MnO_x + 100 x ZrO_2 samples (100+100 sample/film) (Fig. 11-c). This is also shown in Figure 12, in which the memory maps [68] drawn from the same films are depicted. This fact can be explained taking into account that the number of ALD cycles determines the thickness of the film (14 nm versus 36 nm, in this case). The 100+100 film also demonstrated the narrowest window together with the multilayer film, which consisted of five sequential layers in stack. In addition to the thickness values (36 nm and 35 nm respectively), this might be due to the existence of several interfaces between the constituent layers, which could hinder the formation of the conductive filament.

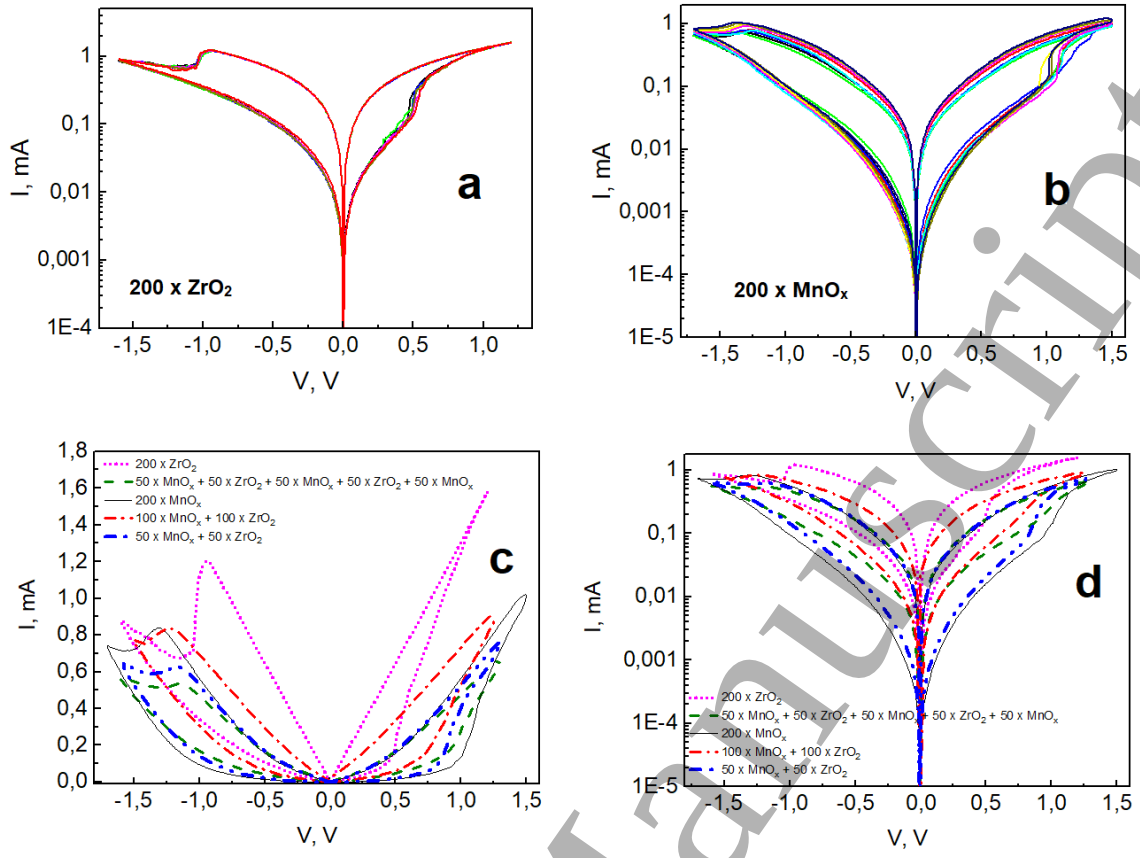

Figure 11. Current – Voltage cycles of pure ZrO_2 (a), and MnO_x (b) samples, and average current-voltage loops of all the films on a linear scale (c) and on a logarithmic scale (d).

The non-laminated ZrO_2 film had the lowest SET and RESET voltages (Fig. 11-a). However, this film was also the one with the highest current values for both LRS and HRS states (see also Fig. 12-a), showing, at the same time, the steepest SET and RESET transitions. At first glance, this could be seen as an advantage, as these transitions are also the fastest of all the samples. Nevertheless, this steep transition implies that ZrO_2 samples alone may not perform well in multilevel applications, and the high current values may simply make it the least suitable for non-volatile-memory applications, as the power consumption would remain high. The results for non-laminated ZrO_2 results are in a good accordance with the ones presented earlier by Ossorio et al. [69].

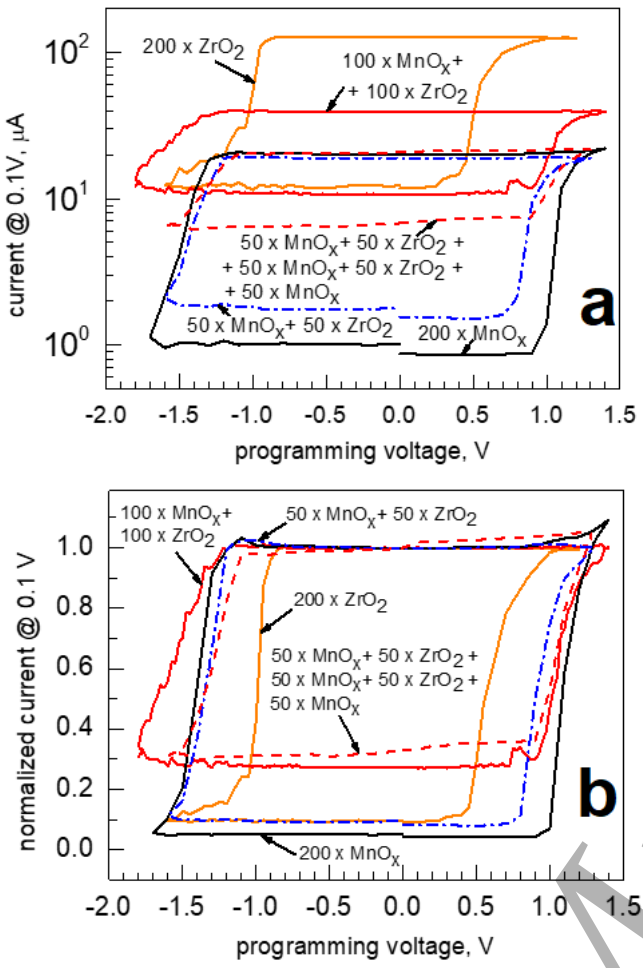

Figure 12. Memory maps (a) and normalized memory maps (b) of the different samples. These maps are obtained by reading the current at 0.1 V after applying a previous programming voltage. The normalized values are obtained by considering the LRS as a value of 1.0.

The non-laminated MnO_x sample the lowest current values for both high and low resistance states (Figs. 11-b, 11-c), which provide similar resistance values to those determined by Zhang et al. [70] when applying Ohm's law to the current values obtained for both HRS and LRS in the memory map that can be seen in Figure 12. The memory maps are an image of the state of the RRAM cell after a previous stress stimulus, and are obtained by measuring some representative magnitude of the state at voltages low enough so that the measurement process itself does not alter the state of the device [68, 71].

The low current values, along with a notably wide functional window (Fig. 12-b), make the MnO_x film the most adequate for memory applications. Additionally, this sample presented smooth SET and RESET transitions, thus showing multilevel capabilities, which have been

demonstrated to be useful for neuromorphic applications, i.e., artificial neural networks, as they might behave as electronic synapses [72].

The latter is also true for the MnO_x-ZrO_2 mixed samples, which all presented smooth SET and RESET transitions, as well as lower HRS and LRS currents when comparing them to the non-laminated ZrO_2 film. Thus, MnO_x-ZrO_2 films might become further investigated and suited to multilevel applications, as implied especially by the 100+100 sample film, which demonstrated the smoothest transitions. On the other hand, these stacks possessed rather narrow functional windows and, consequently, may not regarded as the most appropriate for memory applications, with the exception of the 50+50 sample, which really exhibited high ratio between HRS and LRS as well as appreciably low current values.

Summary

ZrO_2 and manganese oxide films, as well as their layered structures, were deposited by ALD, using $ZrCl_4$, $Mn(acac)_3$ and ozone. XPS results confirmed significant contribution from carbon containing species in the manganese oxide film deposited at 250 °C, allowing one to consider even the formation and presence of $MnCO_3$. At the same time, in the film deposited at 300 °C, essentially weaker role for residual carbon, and formation of Mn_3O_4 was detected and determined by both XPS and GIXRD. Therefore, 300 °C was chosen for the deposition temperature for nanolaminates. Non-laminated ZrO_2 was found to form in its cubic and tetragonal polymorphs, whereas non-laminated manganese oxide possessed cubic Mn_2O_3 and tetragonal Mn_3O_4 phases. All the films were found to behave as ferromagnetic-like materials. At the same time, hysteretic charge polarization – electric field behaviour was not registered, and also the Double Swing Quiescent Current method measurements did not imply any ferroelectric behaviour. Manganese oxide films demonstrated both saturation magnetization and coercivity values by two orders of magnitude higher at 5 K, compared to the values measured at 300 K. In ZrO_2-MnO_x films and nanolaminates, the polarization values at the aforementioned temperatures reached differed by about ten times. Manganese oxide lost its high magnetization value at 40-45 K.

All films exhibited excellent resistive switching characteristics with almost no difference between their commutation values. However, there appeared remarkable differences in the current values linked to both high and low resistance states, with the non-laminated ZrO_2 sample film showing the highest ratios between these states. The non-laminated MnO_x film

possessed the lowest ratio, while in the different ZrO_2-MnO_x samples the ratio between high and low resistance states varied. Both non-laminated samples present great functional windows between each resistance state. Nevertheless, the mixed ZrO_2-MnO_x films have very different windows between these states, with the 50 x MnO_x + 50 x ZrO_2 showing a great functional window, while the 100 x MnO_x + 100 x ZrO_2 and the multilayer film show the narrowest windows. This is explained by the variation in thickness and the fact that the multiple interfaces between the layer could hinder the formation of the filament. These results prove the potential interest of the MnO_x and ZrO_2/MnO_x-based MIM structures in both non-volatile memories and neuromorphic applications.

Acknowledgements

The present study was partially funded by the European Regional Development Fund projects “Emerging orders in quantum and nanomaterials” (TK134), "Advanced materials and high-technology devices for sustainable energetics, sensorics and nanoelectronics“ (TK141), Spanish Ministry of Economy and Competitiveness (TEC2017-84321-C4-2-R) with support of Feder funds and Estonian Research Agency (PRG4, PRG753).

References

1. Gottmann J and Kreutz E W 1999 Pulsed laser deposition of alumina and zirconia thin films on polymers and glass as optical and protective coatings *Surface and Coatings Technology* **116-119** 1189-1194. https://doi.org/10.1016/S0257-8972(99)00191-7

2. Edlou S M, Smajkiewicz A, Al-Jumaily G A 1993 Optical properties and environmental stability of oxide coatings deposited by reactive sputtering *Appl. Opt.* **32** 5601-5605. https://doi.org/10.1364/AO.32.005601

3. Sorek Y, Zevin M, Reisfeld R, Hurvits T and Ruschin S 1997 Zirconia and Zirconia−ORMOSIL Planar Waveguides Prepared at Room Temperature *Chem. Mater.* **9** 670–676. https://doi.org/10.1021/cm960135x

4. Jasieniak J, Pacifico J, Signorini R, Chiasera A, Ferrari M, Martucci A and Mulvaney P 2007 Luminescence and Amplified Stimulated Emission in CdSe–ZnS-Nanocrystal-Doped

TiO_2 and ZrO_2 Waveguides *Advanced Functional Materials* **17** 1654-1662. https://doi.org/10.1002/adfm.200600955

5. Okamoto H, Obayashi H and Kudo T 1980 Carbon monoxide gas sensor made of stabilized zirconia *Solid State Ionics* **1** 319-326. https://doi.org/10.1016/0167-2738(80)90012-0

6. Miura N, Nakatou M and Zhuiykov S 2003 Impedancemetric gas sensor based on zirconia solid electrolyte and oxide sensing electrode for detecting total NO_x at high temperature *Sensors and Actuators B: Chemical* **93** 221-228. https://doi.org/10.1016/S0925-4005(03)00196-5

7. Houssa M, Afanasiev V V, Stesmans A and Heyns M M 2000 Variation in the fixed charge density of SiO_x/ZrO_2 gate dielectric stacks during postdeposition oxidation *Appl. Phys. Lett.* **77** 1885-1887. https://doi.org/10.1063/1.1310635

8. Lin C Y, Wang S Y, Lee D Y and Tseng T Y 2008 Electrical properties and fatigue behaviors of ZrO_2 resistive switching thin films *Journal of The Electrochemical Society* **155** H615-H619. https://doi.org/10.1149/1.2946430

9. Müller J, Böscke T S, Schröder U, Mueller S, Bräuhaus D, Böttger U, Frey L and Mikolajick T 2012 Ferroelectricity in Simple Binary ZrO_2 and HfO_2 *Nano Letters* **12** 4318-4323. https://doi.org/10.1021/nl302049k

10. Weeks S L, Pal A, Narasimhan V K, Littau K A and Chiang T 2017 Engineering of Ferroelectric HfO_2–ZrO_2 Nanolaminates *ACS Appl. Mater. Interfaces* **9** 13440–13447. https://doi.org/10.1021/acsami.7b00776

11. Jia X, Yang W, Qin M and Li J 2009 Structure and magnetism in Mn-doped zirconia: Density-functional theory studies *Journal of Magnetism and Magnetic Materials* **321** 2354-2358. https://doi.org/10.1016/j.jmmm.2009.02.132

12. Dimri M C, Kooskora H, Pahapill J, Joon E, Heinmaa I, Subbi J and Stern R 2011 Search for ferromagnetism in manganese-stabilized zirconia *Physica Status Solidi A - Applications and Materials Science* **208** 172-179. https://doi.org/10.1002/pssa.201026304

13. Hong N H, Kanoun M B, Goumri-Said S, Song J H, Chikoidze E, Dumont Y, Ruyter A and Kurisu M 2013 The origin of magnetism in transition metal-doped ZrO_2 thin films: experiment and theory *Journal of Physics: Condensed Matter* **25** 436003. https://doi.org/10.1088/0953-8984/25/43/436003

14. Dimri M C, Khanduri H, Kooskora H, Kodu M, Jaaniso R, Heinmaa I, Mere A, Krustok J and Stern R 2012 Room-temperature ferromagnetism in Ca and Mg stabilized cubic zirconia *Journal of Physics D - Applied Physics* **45** 475003. https://doi.org/10.1088/0022-3727/45/47/475003

15. Chouhan L, Bouzerar G and Srivastava S K 2020 d(0) Ferromagnetism in Ag-doped monoclinic ZrO_2 compounds *Vacuum* **182** 109716. https://doi.org/10.1016/j.vacuum.2020.109716

16. Ning S, Zhan P, Xie Q, Li Z and Zhang Z 2013 Room-temperature ferromagnetism in un-doped ZrO2 thin films *Journal of Physics D: Applied Physics* **46** 445004. https://doi.org/10.1088/0022-3727/46/44/445004

17. Pattanaik S, Mishra D K, Sharma M K and Chatterjee R 2020 Experimental evidences of ferromagnetism in undoped monoclinic zirconia *Inorganic Chemistry Communications* **118** 108042. https://doi.org/1016/j.inoche.2020.108042

18. Oyama S T 2000 Chemical and catalytic properties of ozone *Catalysis Reviews* **42** 279-322. https://doi.org/10.1081/CR-100100263

19. Torresi S C and Gorenstrein A 1992 Electrochromic behaviour of manganese dioxide electrodes in slightly alkaline solutions *Electrochimica acta* **37** 2015-2019. https://doi.org/10.1016/0013-4686(92)87117-I

20. Strandwitz N C, Comstock D J, Grimm R L, Nichols-Nielander A C, Elam J and Lewis N S 2013 Photoelectrochemical behavior of n-type Si (100) electrodes coated with thin films of manganese oxide grown by atomic layer deposition *The Journal of Physical Chemistry C* **117** 4931-4936. https://doi.org/10.1021/jp311207x

21. Mattelaer F, Bosserez T, Rongé J, Martens J A, Dendooven J and Detavernier C 2016 Manganese oxide films with controlled oxidation state for water splitting devices through a combination of atomic layer deposition and post-deposition annealing *RSC advances* **6** 98337-98343. https://doi.org/10.1039/C6RA19188F

22. Gao P, Meng L J, Dos Santos M P, Teixeira V and Andritschky M 2000 Characterisation of ZrO_2 films prepared by rf reactive sputtering at different O_2 concentrations in the sputtering gases *Vacuum* **56** 143-148. https://doi.org/10.1016/S0040-6090(00)01395-X

23. Landorf R W and Licht S J 1972 Sputtered Manganese Dioxide as Counterelectrodes in Thin Film Capacitors *Journal of The Electrochemical Society* **119** 430. https://doi.org/10.1149/1.2404223

24. Neubeck W, Ranno L, Hunt M B, Vettier C and Givord D 1999 Epitaxial MnO thin films grown by pulsed laser deposition *Applied surface science* **138** 195-198. https://doi.org/10.1016/S0169-4332(98)00421-8

25. Shen Y, Shao S, Yu H, Fan Z, He H and Shao J 2007 Influences of oxygen partial pressure on structure and related properties of ZrO_2 thin films prepared by electron beam evaporation deposition *Applied surface science* **254** 552-556. https://doi.org/10.1016/j.apsusc.2007.06.029

26. Seike T and Nagai J 1991 Electrochromism of 3d transition metal oxides *Solar energy materials* **22** 107-117. https://doi.org/10.1016/0165-1633(91)90010-I

27. Jeon T S, White J M, Kwong D L 2001 Thermal stability of ultrathin ZrO_2 films prepared by chemical vapor deposition on Si (100) *Applied Physics Letters* **78** 368-370. https://doi.org/10.1063/1.1339994

28. Rizzi G A, Zanoni R, Di Siro S, Perriello L and Granozzi G 2000 Epitaxial growth of MnO nanoparticles on Pt (111) by reactive deposition of $Mn_2(CO)_{10}$ *Surface science* **462** 187-194. https://doi.org/10.1016/S0039-6028(00)00608-7

29. Perednis D, Wilhelm O, Pratsinis S E and Gauckler L J 2005 Morphology and deposition of thin yttria-stabilized zirconia films using spray pyrolysis *Thin solid films* **474** 84-95. https://doi.org/10.1016/j.tsf.2004.08.014

30. Valletta R M and Pliskin W A 1967 Preparation and characterization of manganese oxide thin films *Journal of The Electrochemical Society* **114** 944. https://doi.org/10.1149/1.2426786

31. Kukli K, Niinistö J, Tamm A, Lu J, Ritala M, Leskelä M and Putkonen M 2007 Atomic layer deposition of ZrO_2 and HfO_2 on deep trenched and planar silicon *Microelectronic engineering* **84** 2010-2013. https://doi.org/10.1016/j.mee.2007.04.035

32. Aarik L, Alles H, Aidla A, Kahro T, Kukli K, Niinistö J and Mändar H Influence of process parameters on atomic layer deposition of ZrO_2 thin films from $CpZr(NMe_2)_3$ and H_2O *Thin Solid Films* **565** 37-44. https://doi.org/10.1016/j.tsf.2014.06.052

33. Kim H, McIntyre P C and Saraswat K C 2004 Microstructural evolution of ZrO_2–HfO_2 nanolaminate structures grown by atomic layer deposition *Journal of materials research* **19** 643-650. https://doi.org/10.1557/jmr.2004.19.2.643

34. Tamm A, Kozlova J, Aarik L, Aidla A, Lu J, Kiisler A A, Kasikov A, Ritslaid P, Mändar H, Hultman L, Sammelselg V, Kukli K and Aarik J 2014 Atomic layer deposition of ZrO_2 for graphene-based multilayer structures: In situ and ex situ characterization of growth process *physica status solidi (a)* **211** 397-402. https://doi.org/10.1002/pssa.201330106

35. Lin Y C, McGuire F and Franklin A D 2018 Realizing ferroelectric $Hf_{0.5}Zr_{0.5}O_2$ with elemental capping layers *Journal of Vacuum Science & Technology B, Nanotechnology and Microelectronics: Materials, Processing, Measurement, and Phenomena* **36** 011204. https://doi.org/10.1116/1.5002558

36. Nilsen O, Fjellvåg H and Kjekshus A 2003 Growth of manganese oxide thin films by atomic layer deposition *Thin Solid Films* **444** 44-51. https://doi.org/10.1016/S0040-6090(03)01101-5

37. Ghods A, Zhou C and Ferguson I T 2020 Structural and optical properties of (Zn, Mn) O thin films prepared by atomic layer deposition *Journal of Vacuum Science & Technology A: Vacuum, Surfaces, and Films* **38** 042408. https://doi.org/10.1116/6.0000141

38. Arroval T, Aarik L, Rammula R, Kruusla V and Aarik J 2016 Effect of substrate-enhanced and inhibited growth on atomic layer deposition and properties of aluminum–titanium oxide films *Thin Solid Films* **600** 119–125. http://dx.doi.org/10.1016/j.tsf.2016.01.024

39. Kalam K, Seemen H, Ritslaid P, Rähn M, Tamm A, Kukli K, Kasikov A, Link J, Stern R, Dueñas S and Castán H 2018 Atomic layer deposition and properties of ZrO_2/Fe_2O_3 thin films *Beilstein Journal of Nanotechnology* **9** 119-128. http://dx.doi.org/10.3762/bjnano.9.14

40. Granneman E, Fischer P, Pierreux D, Terhorst H and Zagwijn P 2007 Batch ALD: Characteristics, comparison with single wafer ALD, and examples *Surface and coatings technology* **201** 8899-8907. https://doi.org/10.1016/j.surfcoat.2007.05.009

41. Zagwijn P M, Verweij W, Pierreux D, Adjeroud N, Bankras R, Oosterlaken E, Snijders G J, Van den Hout M, Fischer P, Wilhelm R and Knapp M 2008 Novel Batch Titanium Nitride CVD Process for Advanced Metal Electrodes *ECS Transactions* **13** 459. https://doi.org/10.1149/1.2911530

42. Fairley N 2018 CasaXPS: Processing Software for XPS, AES, SIMS and More (Casa Software Ltd., 2018) [online] http://www.casaxps.com/. [Google Scholar]

43. Castán H, Dueñas S, García H, Ossorio O G, Domínguez L A, Sahelices B, Miranda E, González M B and Campabadal F 2018 Analysis and control of the intermediate memory states of RRAM devices by means of admittance parameters *Journal of Applied Physics* **124** 152101. https://doi.org/10.1063/1.5024836

44. Castán H, Dueñas S, Kukli K, Kemell M, Ritala M and Leskelä M 2018 Study of the influence of the dielectric composition of Al/Ti/ZrO_2:Al_2O_3/TiN/Si/Al structures on the resistive switching behavior for memory applications *ECS Transactions* **85** 143-148. https://doi.org/10.1149/08508.0143ecst

45. Dueñas S, Castán H, Ossorio O G, Vinuesa G, García H, Kukli K and Leskelä K 2020 Double Swing Quiescent-Current: An Experimental Detection Method of Ferroelectricity in Very Leaky Dielectric Films *ECS Transactions* **97** 3-6. https://doi.org/10.1149/09701.0003ecst

46. Ritala M and Leskelä M 1994 Zirconium dioxide thin films deposited by ALE using zirconium tetrachloride as precursor *Applied Surface Science* **75** 333-340. https://doi.org/10.1016/0169-4332(94)90180-5

47. Siimon H and Aarik J 1997 Thickness profiles of thin films caused by secondary reactions in flow-type atomic layer deposition reactors *Journal of Physics D: Applied Physics* **30** 1725. https://doi.org/10.1088/0022-3727/30/12/006

48. Bocquet A E, Mizokawa T, Morikawa K, Fujimori A, Barman S R, Maiti K, Sarma D D, Tokura Y and Onoda M 1996 Electronic structure of early 3d-transition-metal oxides by analysis of the 2p core-level photoemission spectra *Phys. Rev. B* **53** 1161. https://doi.org/10.1103/PhysRevB.53.1161

49. NIST X-ray Photoelectron Spectroscopy Database, NIST Standard Reference Database Number 20, National Institute of Standards and Technology, Gaithersburg MD, 20899 (2000), https://doi.org/10.18434/T4T88K, (retrieved Nov. 22, 2020).

50. Stranick M A 1999 MnO_2 by XPS *Surface Science Spectra* **6** 31. https://doi.org/10.1116/1.1247888

51. Stranick M A 1999 Mn_2O_3 by XPS *Surface Science Spectra* **6** 39. https://doi.org/10.1116/1.1247889

52. Yamamoto S, Bluhm H, Andersson K, Ketteler G, Ogasawara H, Salmeron M and Nilsson A 2008 In situ x-ray photoelectron spectroscopy studies of water on metals and oxides at ambient conditions *J. Phys.: Condens. Matter* **20** 184025. https://doi.org/10.1088/0953-8984/20/18/184025

53. Shi S, Zhang M, Deng T, Wang T and Yang G 2017 A facile strategy to construct binder-free flexible carbonate composite anode at low temperature with high performances for lithium-ion batteries *Electrochimica Acta* **246** 1004-1015. https://doi.org/10.1016/j.electacta.2017.06.135

54. Zhang Y X and Jia Y 2018 Fluoride adsorption on manganese carbonate: Ion-exchange based on the surface carbonate-like groups and hydroxyl groups *Journal of Colloid and Interface Science* **510** 407-417. https://doi.org/10.1016/j.jcis.2017.09.090

55. Stranick M A 1999 $Mn(C_2H_3O_2)_2$ by XPS *Surface Science Spectra* **6** 47. https://doi.org/10.1116/1.1247893

56. Fadley C S, Shirley D A, Freeman A J, Bagus P S and Mallow J W 1969 Multiplet Splitting of Core-Electron Binding Energies in Transition-Metal Ions *Phys. Rev. Lett.* **23** 1397. https://doi.org/10.1103/PhysRevLett.23.1397

57. Takahashi M and Igarashi J 2010 Ab initio study of 3s core-level x-ray photoemission spectra in transition metals *Phys. Rev. B* **81** 035118. https://doi.org/10.1103/PhysRevB.81.035118

58. Galakhov V R, Demeter M, Bartkowski S, Neumann M, Ovechkina N A, Kurmaev E Z, Lobachevskaya N I, Mukovskii Y M, Mitchell J and Ederer D L 2002 Mn 3s exchange splitting in mixed-valence manganites *Phys. Rev. B* **65** 113102. https://doi.org/10.1103/PhysRevB.65.113102

59. Ilton E S, Post J E, Heaney P J, Ling F T and Kerisit S N 2016 XPS determination of Mn oxidation states in Mn (hydr)oxides *Applied Surface Science* **366** 475-485. https://doi.org/10.1016/j.apsusc.2015.12.159

60. Kalam K, Seemen H, Mikkor M, Ritslaid P, Stern R, Duenas S, Castan H, Tamm A and Kukli K 2018 Electric and Magnetic Properties of Atomic Layer Deposited ZrO_2-HfO_2 Thin

Films *ECS Journal of Solid State Science and Technology* **7** N117. https://doi.org/10.1149/2.0041809jss

61. Sangalli D, Cianci E, Lamperti A, Ciprian R, Albertini F, Casoli F, Lupo P, Nasi L, Campanini M and Debernardi A 2013 Exploiting magnetic properties of Fe doping in zirconia *The European Physical Journal B* **86** 211. https://doi.org/10.1140/epjb/e2013-30669-3

62. Thota S, Prasad B, Kumar J 2010 Formation and magnetic behaviour of manganese oxide nanoparticles *Materials Science and Engineering B* **167** 153–160. https://doi:10.1016/j.mseb.2010.01.049

63. Liu C, Yun F and Morkoc H 2005 Ferromagnetism of ZnO and GaN: a review *Journal of Materials Science: Materials in Electronics* **16** 555. https://doi.org/10.1007/s10854-005-3232-1

64. Moharreri E, Hines W A, Biswas S, Perry D M, He J, Murray-Simmons D and Suib S L 2018 Comprehensive magnetic study of nanostructured mesoporous manganese oxide materials and implications for catalytic behavior *Chemistry of Materials* **30** 1164-1177. https://doi.org/10.1021/acs.chemmater.7b05280

65. Wang Z H, Geng D Y, Hu W J, Ren W J, Zhang Z D 2009 Magnetic properties and exchange bias in Mn_2O_3/Mn_3O_4 nanoclusters *Journal of Applied Physics* **105** 07A315. https://doi.org/10.1063/1.3055349

66. Waser R, Dittmann R, Staikov G and Szot K 2009 Redox-Based Resistive Switching Memories – Nanoionic Mechanisms, Prospects, and Challenges *Advanced Materials* **21** 3754. https://doi.org/10.1002/adma.200900375

67. Yang J J, Miao F, Pickett M D, Ohlberg D A A, Stewart D R, Lau C N and Williams R S 2009 The mechanism of electroforming of metal oxide memristive switches *Nanotechnology* **20** 215201. https://doi.org/10.1088/0957-4484/20/21/215201

68. Dueñas S, Castán H, Kukli K, Mikkor M, Kalam K, Arroval T and Tamm A 2018 Memory Maps: Reading RRAM Devices without Power Consumption *ECS Transactions* **85** 201. https://doi.org/10.1149/08508.0201ecst

69. Ossorio O G, Dueñas S, Castán H, Tamm A, Kalam K, Seemen H and Kukli K 2019 Resistive Switching Properties of Atomic Layer Deposited ZrO_2-HfO_2 Thin Films *Spanish Conference on Electron Devices (CDE)* 1-4. https://doi.org/10.1109/CDE.2018.8596925

70. Zhang S, Long S, Guan W, Liu Q, Wang Q and Liu M 2009 Resistive switching characteristics of MnO_x-based ReRAM *Journal of Physics D: Applied Physics* **42** 055112. https://doi.org/10.1088/0022-3727/42/5/055112

71. Castán H, Dueñas S, García H, Ossorio O G, Domínguez L A, Sahelices B, Miranda E, González M B and Campabadal F 2018 Analysis and control of the intermediate memory states of RRAM devices by means of admittance parameters *Journal of Applied Physics* **124** 152101. https://doi.org/10.1063/1.5024836

72. Maestro-Izquierdo M, Gonzalez M B and Campadabal F 2019 Mimicking the spike-timing dependent plasticity in HfO_2-based memristors at multiple time scales *Microelectronic Engineering* **215** 111014. https://doi.org/10.1016/j.mee.2019.111014